Article

Fast and Accurate Hyperspectral Image Classification with Window Shape Adaptive Singular Spectrum Analysis

Xiaotian Bai [1,2], Biao Qi [1], Longxu Jin [1,2], Guoning Li [1,2,*] and Jin Li [3]

1   Changchun Institute of Optics, Fine Mechanics and Physics, Chinese Academy of Sciences (CIOMP),
     Changchun 130033, China; baixiaotian19@mails.ucas.edu.cn (X.B.); qibiao@ciomp.ac.cn (B.Q.);
     jinlongxu@ciomp.ac.cn (L.J.)
2   University of Chinese Academy of Sciences, Beijing 100049, China
3   School of Instrumentation and Optoelectronic Engineering, Beihang University, Beijing 100191, China;
     jl11269@buaa.edu.cn
*   Correspondence: liguoning@ciomp.ac.cn

Abstract: Hyperspectral classification is a task of significant importance in the field of remote sensing image processing, with attaining high precision and rapid classification increasingly becoming a research focus. The classification accuracy depends on the degree of raw HSI feature extraction, and the use of endless classification methods has led to an increase in computational complexity. To achieve high accuracy and fast classification, this study analyzes the inherent features of HSI and proposes a novel spectral–spatial feature extraction method called window shape adaptive singular spectrum analysis (WSA-SSA) to reduce the computational complexity of feature extraction. This method combines similar pixels in the neighborhood to reconstruct every pixel in the window, and the main steps are as follows: rearranging the spectral vectors in the irregularly shaped region, constructing an extended trajectory matrix, and extracting the local spatial and spectral information while removing the noise. The results indicate that, given the small sample sizes in the Indian Pines dataset, the Pavia University dataset, and the Salinas dataset, the proposed algorithm achieves classification accuracies of 97.56%, 98.34%, and 99.77%, respectively. The classification speed is more than ten times better than that of other methods, and a classification time of only about 1–2 s is needed.

Keywords: hyperspectral image classification; SSA; adaptive window shape; feature extraction

1. Introduction

The continuous spectral bands of HSI can provide abundant spectral information [1]. HSI incorporates two-dimensional spatial details that depict the relative positioning of various ground objects and the contours of their distribution ranges [2]. HSI classification is the process of assigning the pixels in an image to different categories or land cover types [3]. However, the high correlation of near-continuous band reflectance causes redundancy and overlap in spectral information, which not only increases the computational effort but also reduces the classification accuracy. The limitations of imaging technology create an imbalance between spatial and spectral resolution, with severe interference from both atmospheric transmittance and the weather, which leads to a significant reduction in classification performance [4]. For existing HSI datasets, as the number of data dimensions increases, the number of training samples remains the same, and with a limited number of samples, more statistics need to be estimated. This results in a decline in the accuracy of statistical estimation. While higher spectral dimensionality significantly enhances the separability of classes, it concurrently leads to a reduction in classification accuracy across an unspecified number of bands. This phenomenon is associated with the challenge of dimensionality, commonly known as the Hughes phenomenon [5].

Classification of the raw data presents a great challenge to the performance of the classifier [6]; therefore, HSI classification methods generally consist of two parts: feature extraction and classification judgments [7]. Feature extraction refers to the extraction of the part of the original input data that can optimally represent the original data, which greatly reduces the algorithm complexity without affecting the classification results. In past decades, various HSI classification methods have been proposed; for example, principal component analysis (PCA) [8], independent component analysis (ICA) [9], linear discriminant analysis (LDA) [10], and minimum noise fraction (MNF) [11] are classical methods for feature extraction based on statistical learning theory. It was shown in [12] that the spectral feature curves of HSI exhibit nonlinear properties and a popular structure; as such, many streamline learning methods such as Laplace feature mapping (LEs) [13] and local linear embedding (LLE) [14] have been introduced in the field of HSI feature extraction. In recent years, singular spectrum analysis (SSA) [15] has been applied to HSI feature extraction, and SSA has shown good ability to extract spectral vector features during noise removal. The above methods only perform feature extraction on spectral dimensions without combining spatial information, which imposes some limitations.

Several classical spatial feature extraction methods have been introduced into the field of HSI spatial information feature extraction, such as HSI morphological feature extraction (MP) through morphological transformation [16]. Extended morphological feature extraction (EMP) has also been proposed [17]. In [18,19], attribute filters were employed to replace open and close operations in morphological features, resulting in the extraction of attribute features (AP) and extended attribute features (EAP). The gray-level co-occurrence matrix (GLCM) [20] and wavelet transform (WT) methods [21], and their variants, are classical image processing methods that have also been introduced into the field of HSI spatial feature extraction. A Gabor filter can effectively analyze two-dimensional spatial information, which can then be extended to 3D Gabor [22], a method that can fully represent signal variance in local three-dimensional regions. In recent years, a variety of spectrum feature extraction methods based on graph embedding theory [23] have been proposed. Methods for feature extraction based on spectral perception and local adaptive collaborative representation were proposed in [24,25], respectively, yielding favorable outcomes. Based on SSA, 2DSSA [26] was proposed as a means to extract image spatial information and was superior to many feature extraction algorithms. In [27], 1.5DSSA was proposed as a method for constructing a center pixel containing local spatial information and spectral information according to the Euclidean distance between the center pixel and the center pixel in the small window. In [28], a method combining PCA and SPCA with 2DSSA was proposed as a means to extract multi-scale spatial–spectral features (MSF-PCs). In [29], SpaSSA was proposed as a way to process large pixel blocks with 2DSSA and small pixel blocks with 1DSSA to realize window-size-adaptive SSA and extract local spatial–spectral HSI features. Numerous methods that use spatial feature extraction involve a fixed window traversing each pixel operation, including the center pixel and neighborhood pixel, which not only requires a large amount of computation but also exhibits poor adaptation to irregular shape regions. With the development of deep learning, HSI classification methods based on deep learning have been increasingly proposed [30]. Although the application of methods based on deep convolutional neural networks [31–33] and various attention mechanisms based on transformer networks [34] can extract the deep features of HSI, these methods not only require sophisticated hardware such as a computer but also greatly increase the amount of computation required and cannot complete efficient classification.

To give full play to the performance of SSA in HSI feature extraction, make up for the shortcomings of existing algorithms, reduce the amount of computation, and improve the classification speed, this paper proposes a new adaptive SSA algorithm for the irregular shape region to quickly extract effective spatial–spectral features in HSI. Several experiments on three open data sets and comparisons with other methods show that

the experimental results fully demonstrate the superiority of the algorithm. The main contributions of this paper can be summarized as follows.

(1) The WSA-SSA algorithm is proposed, which is adaptive to the window shape and can extract HSI features for irregularly shaped pixel blocks. The feature map contains both the original data spectral information and local spatial information to improve the classification accuracy.

(2) The spectral vectors in the irregularly shaped window were rearranged, and the scale was selected to construct the trajectory matrix for subsequent processing. Instead of the window sliding pixel by pixel in a certain direction, the calculation amount was reduced, and the HSI image was quickly classified by combining it with the classifier.

(3) Experiments on three datasets show that, in the case of a small number of training samples, the classification performance of the proposed method is superior to several of the most advanced SSA-based methods.

The rest of this paper is organized as follows: The Section 2 introduces the principles of SSA and 2DSSA. The Section 3 describes the HSI classification method based on WSA-SSA. The Section 4 gives the experimental results and the analysis of the experimental results to prove the superiority of the proposed method. Finally, in the Section 5, the thesis is summarized.

2. Related Work

This section introduces the main techniques used in the feature extraction method proposed in this paper, the superpixel segmentation technique, and the principles and methods of traditional SSA. Although SSA and 2DSSA have many drawbacks, the feature extraction method in this paper improves on these two methods and their principles are used in the proposed strategy.

SSA is an eigen-spectrum decomposition method based on the Hankel matrix, which is usually used to deal with nonlinear time series and can analyze and predict time series. It is based on singular value decomposition (SVD) of a specific matrix constructed over a time series, which can be used to decompose the trend, oscillation components, and noise from a time series. SSA has a very wide range of applicability. For time series, neither the parametric model nor stationarity conditions need to be assumed. The process of SSA consists of two complementary phases: decomposition and reconstruction [35]. In the decomposition stage, the SSA algorithm performs a lagged arrangement of the original one-dimensional signal to obtain the trajectory matrix and performs a singular value decomposition of the trajectory matrix to obtain the contribution of each eigenvalue to the trajectory matrix. In the reconstruction stage, the target signal is separated from other signal components and reconstructed according to the signal characteristics using the constraint conditions. In the process of HSI feature extraction, SSA can extract the main trend of the one-dimensional spectral vector. In the SVD step, the first reconstruction component corresponds to the largest eigenvalue and contains the largest amount of original data information, which can roughly replace the raw data [36]. When the EVG value is 1, a better classification effect can be obtained.

2DSSA, like SSA, can extract components such as the trend, oscillation, and noise of a given 2D signal [37]. In [38], the theory of 2DSSA was extended to 2D image processing, and good performance was achieved. 2DSSA extracts its spatial structure features in a similar step to traditional SSA, only the way of constructing the trajectory matrix is different. The trajectory matrix structure constructed by 2DSSA is the Hankel by Hankel (HbH) structure [39]. The subsequent SVD of the constructed trajectory matrix and the subsequent reconstruction operations are similar to the conventional SSA. The 2DSSA method has several advantages in the spatial feature extraction of 2D gray images. Firstly, each lag vector in the constructed trajectory matrix contains local information about the image, while the trajectory matrix as a whole contains global spatial information. In addition, 2DSSA can effectively suppress noise. In HSI, 2DSSA can extract local space features and global space

features. Combined with the spectral feature extraction method, a better classification effect can be obtained.

3. Proposed Method

In this section, we mainly introduce the HSI classification method based on WSA-SSA. The method can be roughly divided into three steps: (1) region division according to the spatial information; (2) spatial–spectral features of HSI extraction based on WSA-SSA; and (3) classification. Figure 1 is a flow diagram of the proposed classification method. The following part describes the three steps in detail.
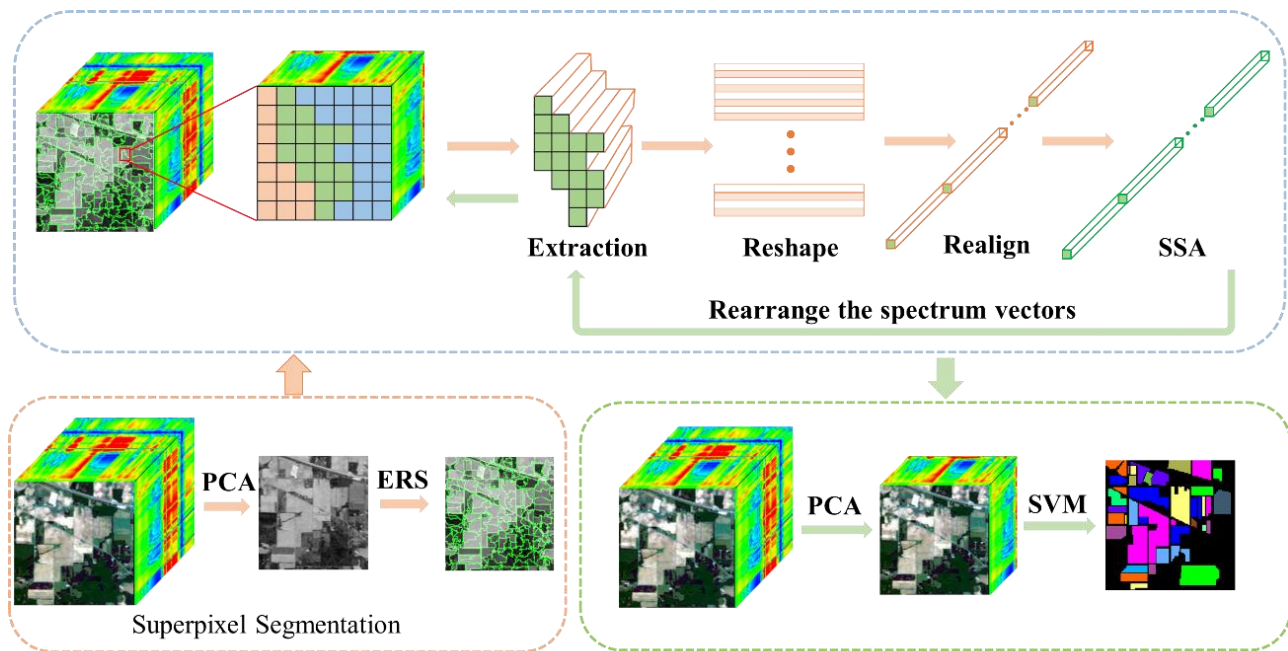

Figure 1. Schematic of the proposed WSA-SSA for the HSI classification framework.

3.1. Region Division Based on Spatial Information

Segmentation of minor regions preserves locally valid information and boundary information of the image. Superpixel segmentation technology can divide pixels with similar characteristics into small areas. Using superpixel to describe image features reduces computational complexity and is generally used as a pre-processing step in image processing [40]. Among the many superpixel segmentation algorithms, the most widely used methods are entropy rate segmentation (ERS) [41] and simple linear iterative clustering (SLIC) [42]. The ERS preserves the boundary information of the image to the greatest extent but generates superpixels with irregular shapes. The shape of the superpixel obtained by the SLIC is more regular, but it partially destroys the boundary information and provides an inaccurate description of the contours. In the process of image preprocessing for HSI classification, the ERS algorithm is used to preprocess the HSI to retain the intact boundary information without affecting the classification results. To reduce the amount of computation, the PCA algorithm is used to reduce the dimension of HSI, the first principal component after dimensionality reduction is segmented by superpixel, and different labels are assigned to different superpixel regions, facilitating subsequent feature extraction and classification.

3.2. WSA-SSA

The ERS method is employed for superpixel segmentation of the first principal component of the Hyperspectral Image (HSI). This process involves partitioning the image into small, irregularly shaped regions based on the first principal component, assigning different labels to distinct regions, and ensuring that pixels within these irregularly shaped

areas share similar characteristics. Features of the HSI are then extracted based on the positions of obtained superpixel labels. The proposed WSA-SSA algorithm in this paper identifies superpixel labels, determines their positions, and records their coordinate locations. The recorded coordinates, selected according to the labels, are located on the HSI, and subsequent calculations are performed only on the regions with the same label. The processed portions, chosen based on the labels, are illustrated in Figure 2.
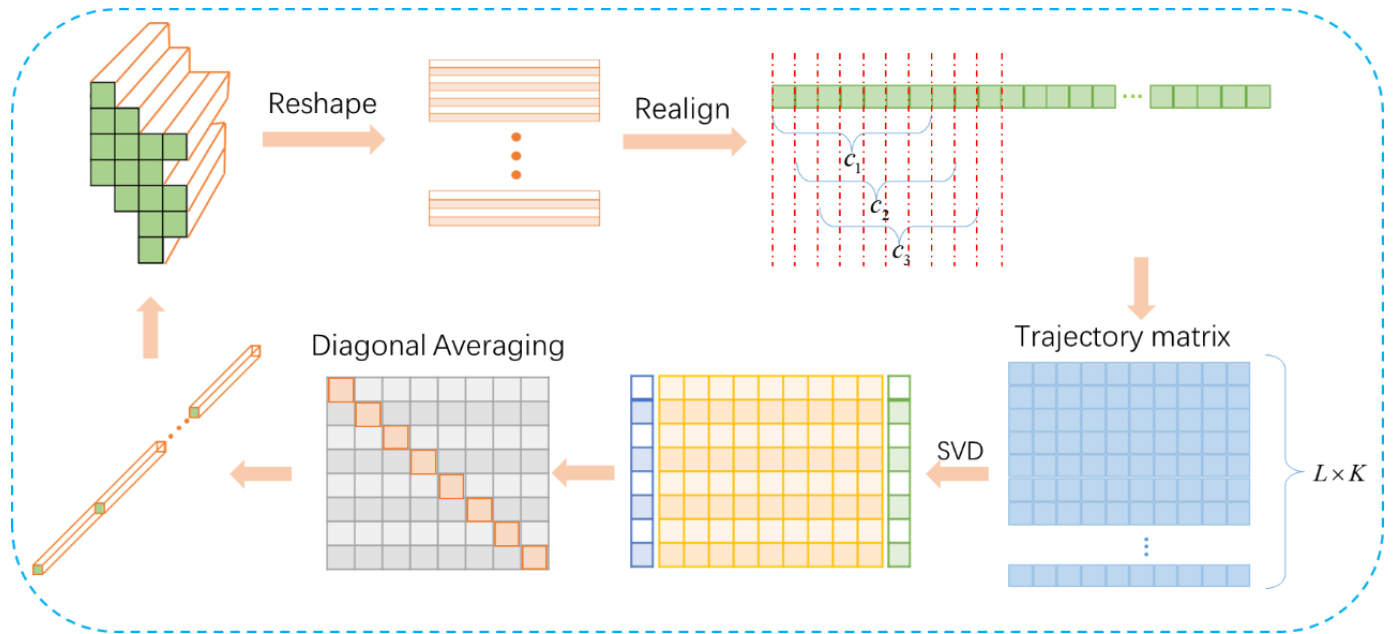

Figure 2. Schematic of the proposed WSA-SSA.

A superpixel is defined as S, consisting of N pixel vectors denoted as $S = \{(x_1, y_1, bands), (x_2, y_2, bands), \ldots, (x_N, y_N, bands)\}$, where (x_i, y_i) is the position coordinate of the pixel in the superpixel and *bands* represents the spectral dimension. Since it is an irregularly shaped superpixel, the pixels in the superpixel are arranged into a one-dimensional spectral vector by the order of coordinate values, denoted as $X = [1, 2, \ldots, B, B + 1, \ldots, N \times B]$, where B is the HSI spectral dimension. The spectral vector contains the local spatial information and spectral information of HSI. $X = [1, 2, \ldots, B, B + 1, \ldots, N \times B]$ is defined as the one-dimensional signal $X = [x_1, x_2, \cdots, x_N] \in R^N$. The appropriate window length $L(1 < L < N)$ is selected to arrange the signal with a lag to obtain the trajectory matrix, and the window size is equal to the number of extracted components. The matrix X is the trajectory matrix of the one-dimensional signal, where $K = N - L + 1$ and the column vector c_i of the trajectory matrix is the lag vector.

$$X = \begin{pmatrix} x_1 & x_2 & \cdots & x_K \\ x_2 & x_3 & \cdots & x_{K+1} \\ \vdots & \vdots & \ddots & \vdots \\ x_L & x_{L+1} & \cdots & x_N \end{pmatrix} = (c_1, c_2, \cdots, c_K) \tag{1}$$

Next, the SVD of the trajectory matrix $X = (c_1, c_2, \cdots c_K)$ is performed. Let $S = XX^T$, $\lambda_1, \lambda_2, \ldots, \lambda_L$ be the eigenvalues, $\lambda_1 \geq \lambda_2 \geq \ldots \geq \lambda_L \geq 0$, and $U_1, U_2, \ldots, U_L$ is the matrix S corresponding to the standard orthogonal vector of these eigenvalues. Let $d = rank(X) = \max\{i, \lambda_i > 0\}$ (note that in the actual sequence, there are usually $d = L^*, L^* = \min\{L, K\}$) and $V_i = X^T U_i / \sqrt{\lambda_i} (i = 1, 2, \ldots, d)$, in which case the SVD of the trajectory matrix can be written as

$$X = X_1 + \ldots + X_d \tag{2}$$

where $X_i = \sqrt{\lambda_i} U_i V_i^T$ is a primitive matrix of rank 1, and U_i and V_i are called the components of the empirical orthogonal function and trajectory matrix, respectively. The matrix is constructed as follows:

$$U = (U_1, U_2 \cdots U_L) \in R^{L \times L} \tag{3}$$

$$V = (V_1, V_2 \cdots V_L) \in R^{L \times L} \tag{4}$$

where $\lambda_i / \sum\limits_{i=1}^{L} \lambda_i$ represents the contribution of the i eigenvalue to the matrix.

In order to separate the target signal components from the other signal components, the set of subscripts $\{1, \cdots, d\}$ is divided into disjoint subsets $I_1, \cdots, I_m$ such that $I = \{i_1, i_2, \cdots, i_P\}$, which corresponds to the synthesis matrix $X_I = X_{i_1} + X_{i_2} + \cdots + X_{i_P}$. After the combination, the trajectory matrix X becomes

$$X = X_{I_1} + X_{I_2} + \cdots + X_{I_m} \tag{5}$$

Transform each matrix X_{I_j} in Equation (5) into a new length sequence N, thus obtaining the decomposed sequence. Let Y be a matrix of $L \times K$ with elements y_{ij}, $1 \leq i \leq L$, and $1 \leq j \leq K$. Let $L^* = \min(L, K)$, $K^* = \max(L, K)$, and $N = L + K - 1$. If $L < K$, then $y_{ij}^* = y_{ij}$; otherwise, $y_{ij}^* = y_{ji}$. Perform diagonal averaging using Equation (6) to transform the matrix N into a sequence $y_1, y_2, \cdots, y_N$.

$$y_k = \begin{cases} \frac{1}{k} \sum\limits_{m=1}^{k} y_m^*, k - m + 1 & for \; 1 \leq k \leq L^* \\ \frac{1}{L^*} \sum\limits_{m=1}^{L^*} y_m^*, k - m + 1 & for \; L^* \leq k \leq K^* \\ \frac{1}{N-k+1} \sum\limits_{m=k-K^*+1}^{N-K^*+1} y_m^*, k - m + 1 & for \; K^* \leq k \leq N \end{cases} \tag{6}$$

The reconstructed feature sequence $y_1, y_2, \cdots, y_N$ is separated into spectral vectors according to the number of pixels and spectral dimensions contained within the superpixel before reconstruction, and the separated spectral vectors are formed into a new superpixel with the same size as the superpixel before feature extraction according to the position coordinates recorded by $S = \{(x_1, y_1, bands), (x_2, y_2, bands), \ldots, (x_N, y_N, bands)\}$. All the small regions are decomposed and reconstructed by the WSA-SSA to form an HSI local spatial–spectral feature image according to the label position of this superpixel, which contains HSI spectral information and local spatial information.

3.3. Classifier

Due to the high spectral dimensionality of HSI, it is still difficult to obtain a large number of training samples based on existing techniques, leading to the Hughes phenomenon in HSI. Due to the robustness of SVM to Hughes phenomenon [43], in the classification stage, SVM with a quintuple cross-validated Gaussian kernel is selected for the final implementation of classification.

4. Experiments and Analysis

To evaluate the extraction ability of the proposed method for the spatial–spectral specialization of HSIs, three basic HSI datasets—Indian Pines, Pavia University, and Salinas— are selected for experiments in this paper. This section presents the three basic datasets, experimental parameter settings, and comparative experimental results.

4.1. Data Set

The three base datasets of Indian Pines, Pavia University, and Salinas were acquired by each mainstream sensor in different scenes with significant differences in the number of bands, spectral resolution, and image size [44]. The detailed parameters are shown in

Table 1, and the pseudo-color, Ground truth, and superpixel segmentation maps of the three datasets are shown in Figures 3–5.

Table 1. Detailed parameters for the dataset.

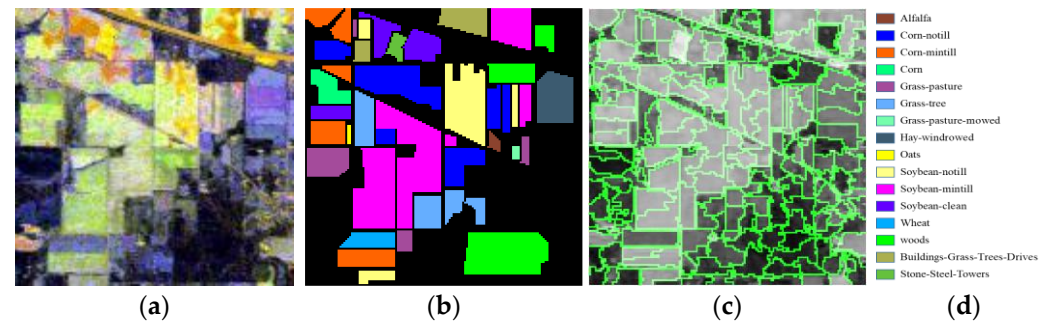| Data	Source	Wavelength Range	Size	Classes
Indian Pines	AVIRIS	0.4~2.5 μm	$145 \times 145 \times 200$	16
Pavia University	ROSIS-03	0.43~0.86 μm	$610 \times 340 \times 103$	9
Salinas	AVIRIS	0.4~2.5 μm	$512 \times 217 \times 204$	16

Figure 3. (**a**) False-color image of the Indian Pines dataset. (**b**) Ground-truth map. (**c**) Segmented map. (**d**) Class names and legend of the different land-cover classes.
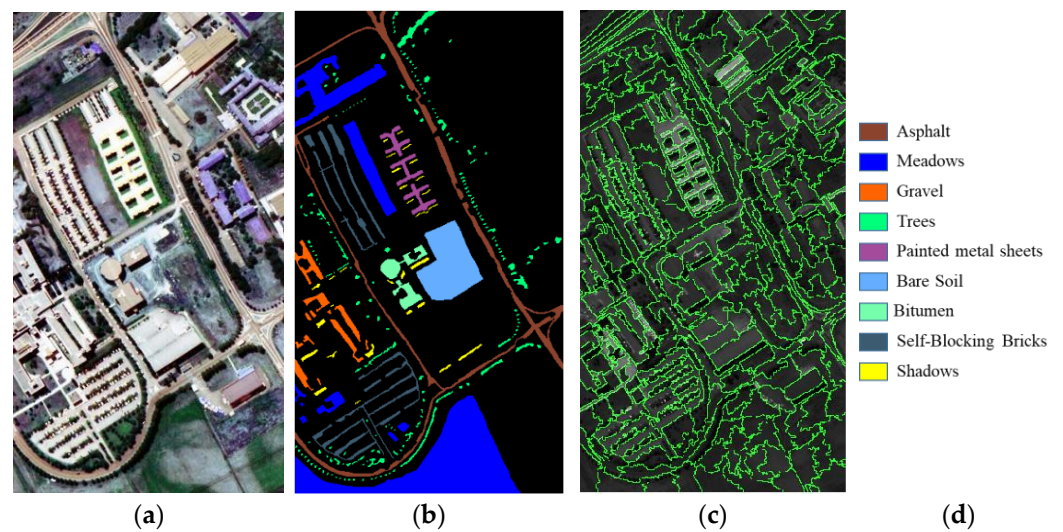

Figure 4. (**a**) False-color image of the Pavia University dataset. (**b**) Ground-truth map. (**c**) Segmented map. (**d**) Class names and legend of the different land-cover classes.

4.2. Parameter Sensitivity Analysis

Two main parameters of WSA-SSA affect the capability of extracting spectral–spatial features, running time, and classification accuracy. To be able to extract rich spatial–spectral features, the window size of WSA-SSA, which is the number of pixels contained in the segmented superpixel, is an important parameter that directly affects the classification accuracy and the running time. The proposed method is improved based on SSA to extract spectral information and local spatial information simultaneously, and its EVG value is fixed to 1. The scale L of SSA is also an important parameter that determines the reconstruction accuracy of the spectral–spatial features of the lagging vector in the trajectory matrix. If the scale is too large, which means the embedding window is too large, it is easy to construct a larger trajectory matrix and increase the computational effort. The scale should not be too small, because the smoothing ability of the data decreases

and the noise-removal ability becomes weaker. The effects of these two parameters on the classification accuracy of the HSI of the three datasets are shown in Figures 6 and 7.
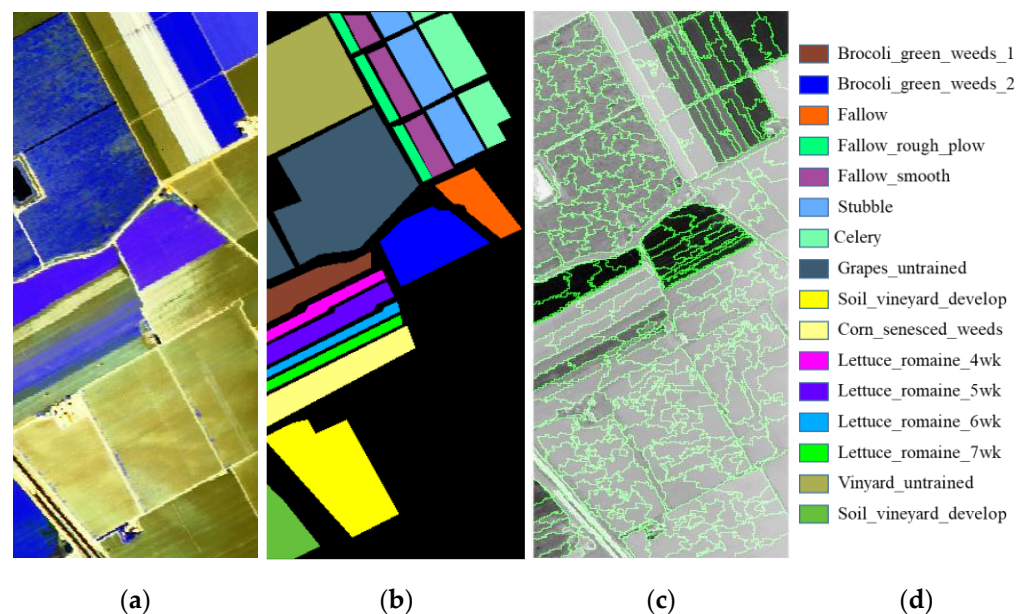

Figure 5. (**a**) False-color image of the Salinas dataset. (**b**) Ground-truth map. (**c**) Segmented map. (**d**) Class names and legend of the different land-cover classes.

The value of the parameter N determines the size of the superpixel, the superpixel area determines the window size of the proposed method, and the arrangement of pixels in the superpixel determines the window shape of the proposed method. The experimental results show that the larger the number of superpixels in a certain range, the higher the classification accuracy obtained. This is because the smaller the segmented superpixel is, the greater the possibility that neighboring pixels belong to the same class of features, and the higher their pixel similarity. By using WSA-SSA to reconstruct the pixels in the area, each pixel contains both its spectral information and the information of pixels with high similarity in the domain, achieving the purpose of obtaining both spectral and local spatial information. Meanwhile, a larger number of superpixels increases the processing times of WSA-SSA but decreases the processing time of single WSA-SSA. The smaller the number of superpixels, the larger the divided area is, the greater the possibility of containing different classes of features in the same area, and the more easily are the reconstructed hyperspectral pixels in its area mixed with information that do not belong to the same class of pixels, which reduces the classification accuracy. At the same time, a smaller number of superpixels reduces the amount of WSA-SSA processing but increases the running time of one WSA-SSA.

The traditional SSA is mostly used to process time series, which only retains the overall trend of the data and easily ignores the higher frequency peaks in the series, and is applied to the processing of HSI spectral vectors, which easily loses the higher frequency peaks in spectral vectors. The experimental results of the effect of scale L of WSA-SSA on the classification accuracy and running time are shown in Figure 7. The variation of scale L within a certain range has a small effect on the classification accuracy and a large effect on the running time. Since the larger the scale L is, and the larger the dimension of the trajectory matrix it constructs, the higher its decomposition is. The larger dimensionality of the trajectory matrix increases the computation volume and prolongs the computation time. The higher the degree of decomposition of the sequence data, the more complete the retention of the components called high frequencies in the spectral vector, but too high a degree of decomposition reduces the ability to eliminate noise. The proposed method rearranges the spectral vectors with high similarity in the superpixel to form the

approximate periodic sequence spectral data, which better exploit the processing capability of the SSA for spectral vectors.
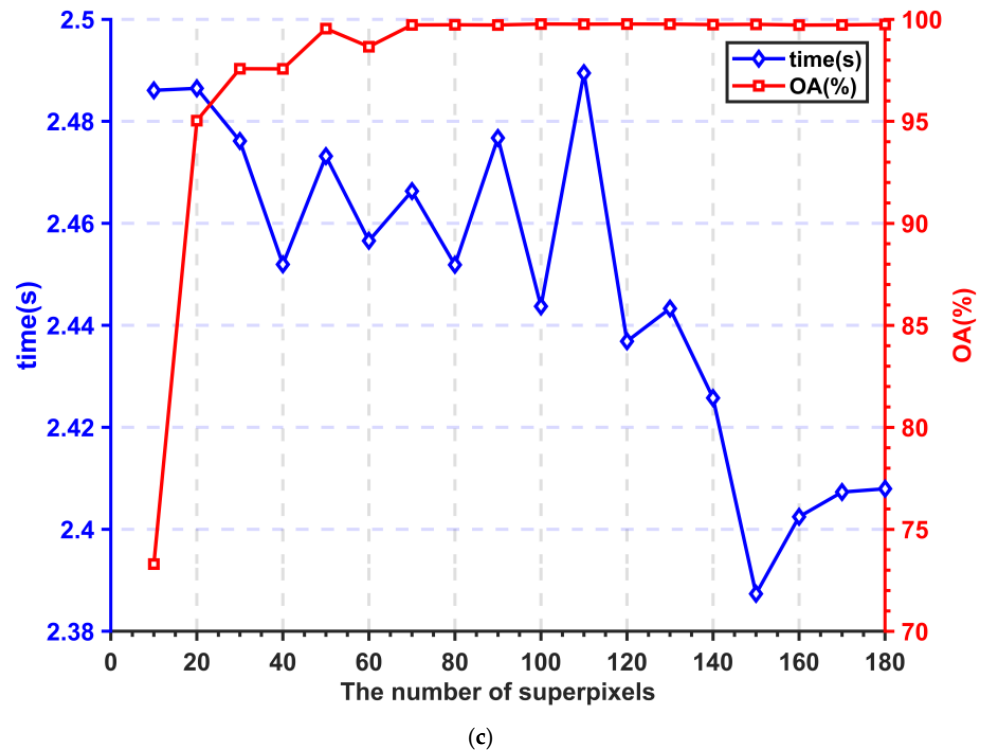

(**a**)

(**b**)

Figure 6. *Cont.*

(**c**)
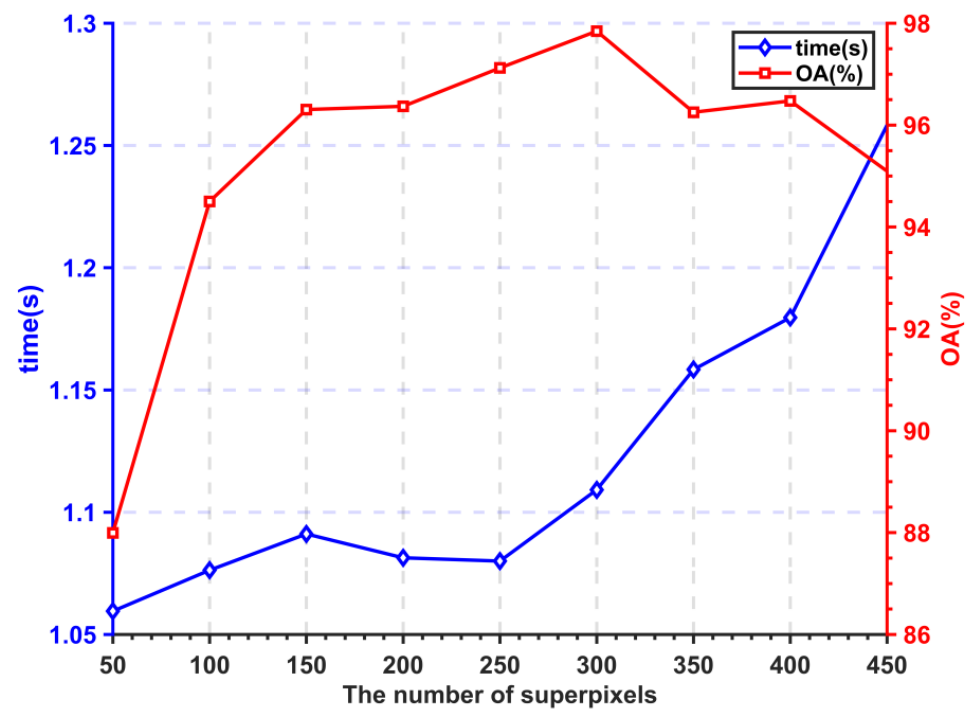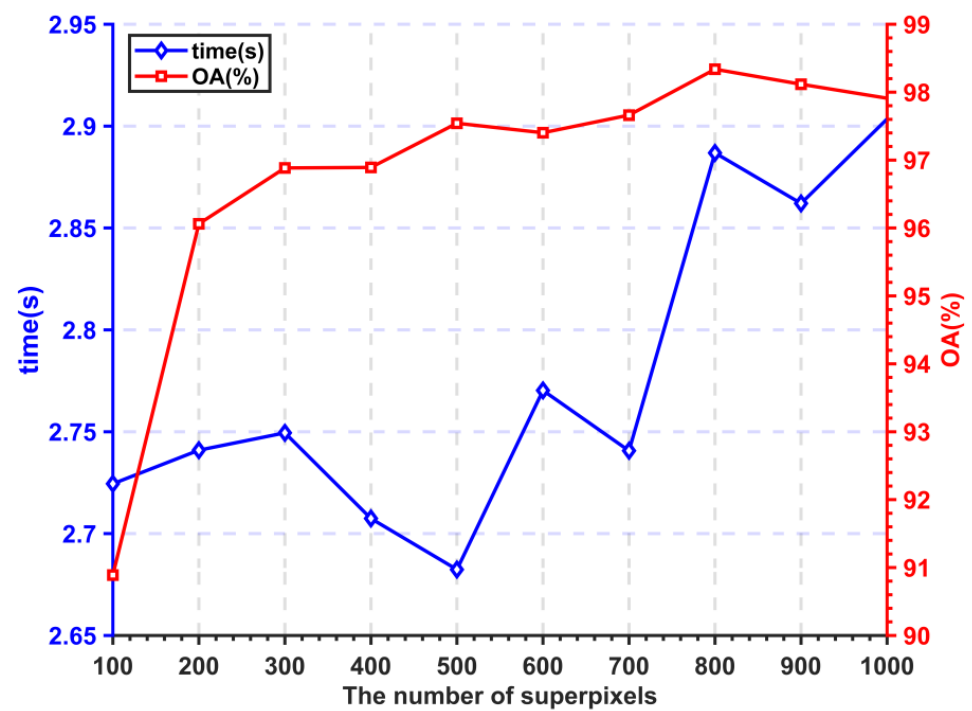
Figure 6. Influence of the parameter N on the classification accuracy and running time of the WSA-SSA on the datasets of (**a**) Indian Pines, (**b**) Pavia University, and (**c**) Salinas.
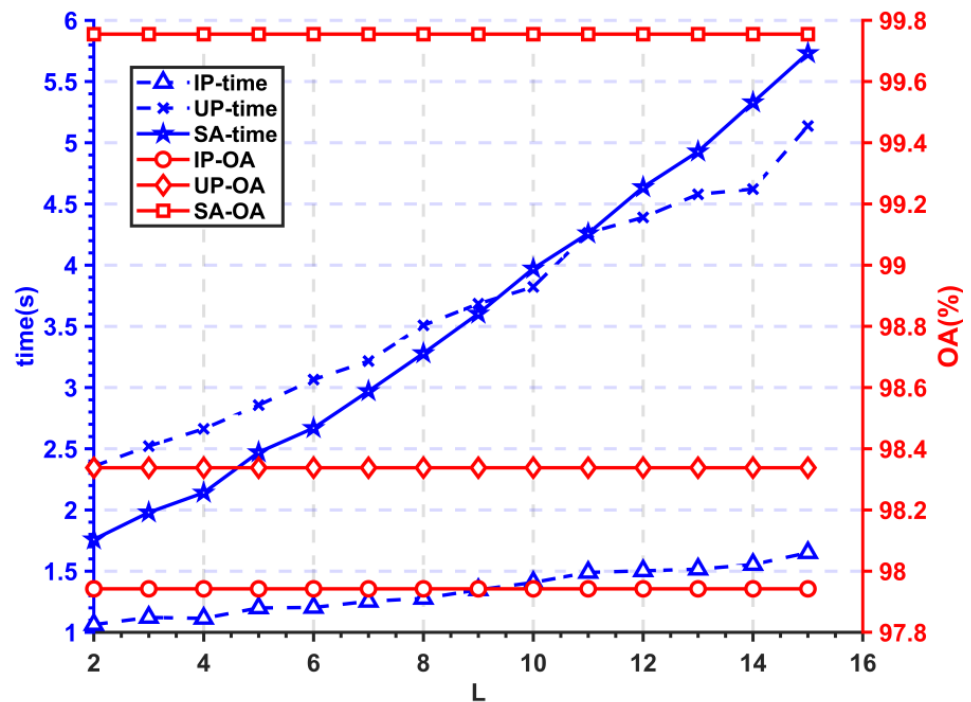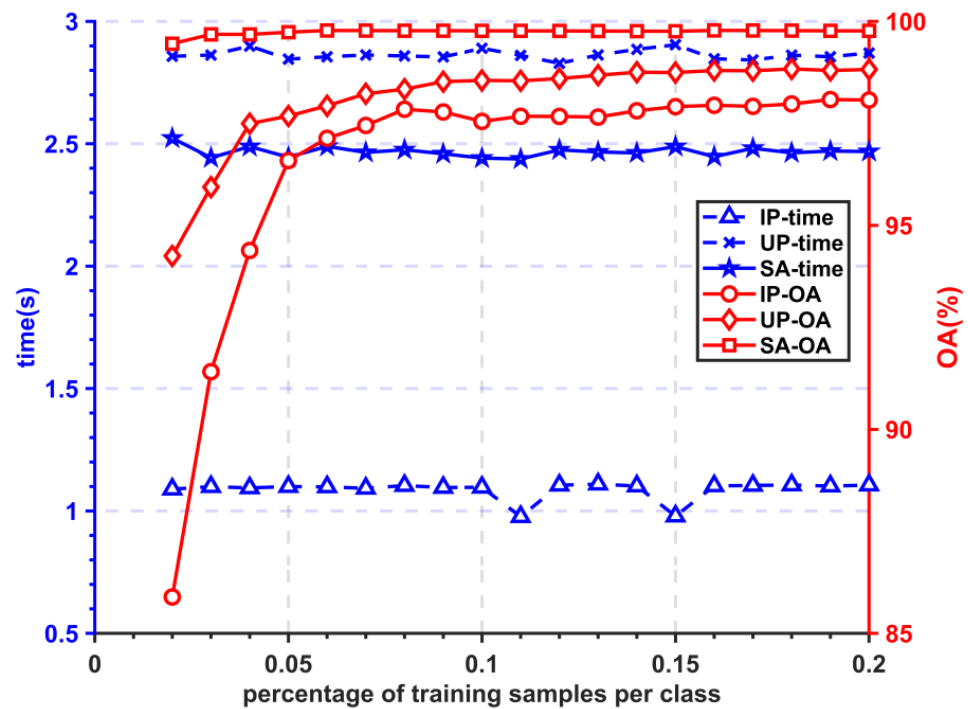

Figure 7. *Cont.*

Figure 7. Influence of the parameter L and the number of training samples on the classification accuracy and running time of the WSA-SSA.

4.3. Comparison Experiments

In this section, the proposed method is experimented on three widely used datasets—Indian Pines, Pavia University, and Salinas—and the performance is compared with some HSI classification methods. To verify the effectiveness of the proposed method, 8% of the labeled samples are randomly selected in each feature type as the training set, and the remaining 92% of the labeled samples are used as the test set. The main methods compared are SVM for the classification of raw data; traditional 1DSSA and 2DSSA combined with SVM, respectively; PCA combined with SVM; and classification methods that have performed better in the last two years. In the experiments, the classifier is selected for the classification method of SVM. The parameters of the Gaussian kernel are uniformly set to $\gamma = 0.125$, $C = 1000$. For the PCA combined with the SVM classification method, the same as the proposed method is chosen for the first 30 components of PCA for classification experiments. For the feature extraction stage, the scale of SSA is $L = 10$ and the window size of 2DSSA is $L \times L = 5 \times 5$. The optimal parameters from their papers were used for MSF-PCs (2020), SpaSSA (2022), NGNMF-E2DSSA (2022) [45], and 1.5D-SSA (2020). To avoid the chance of experimental results, all experiments were performed 10 times with the same equipment, and the results of all numerical indicators are the average of 10 experiments. The effect plots of all the above classification methods are shown in Figures 8–10.

From the classification results, the proposed method achieves very good results on all three datasets. Compared with the SVM, PCA followed by the classification method, and SSA and 2DSSA for feature extraction followed by classification, there is a significant improvement, indicating that the proposed method makes full use of the local spatial and spectral information of HSI to achieve good classification results more easily than using spatial or spectral information alone. Compared with the SpaSSA, NGNMF-E2DSSA, and 1.5D-SSA methods, the proposed method shows obvious advantages in classifying adjacent features. This is because the first three methods use a fixed rectangular window for feature extraction of HSI, followed by SVM for classification. When a fixed shape window is used to traverse each pixel for feature extraction, if the window contains different kinds of feature pixels, it will lead to poor reconstruction accuracy, thus affecting the classification results. The proposed WSA-SSA algorithm, without a fixed shape window, can reconstruct every

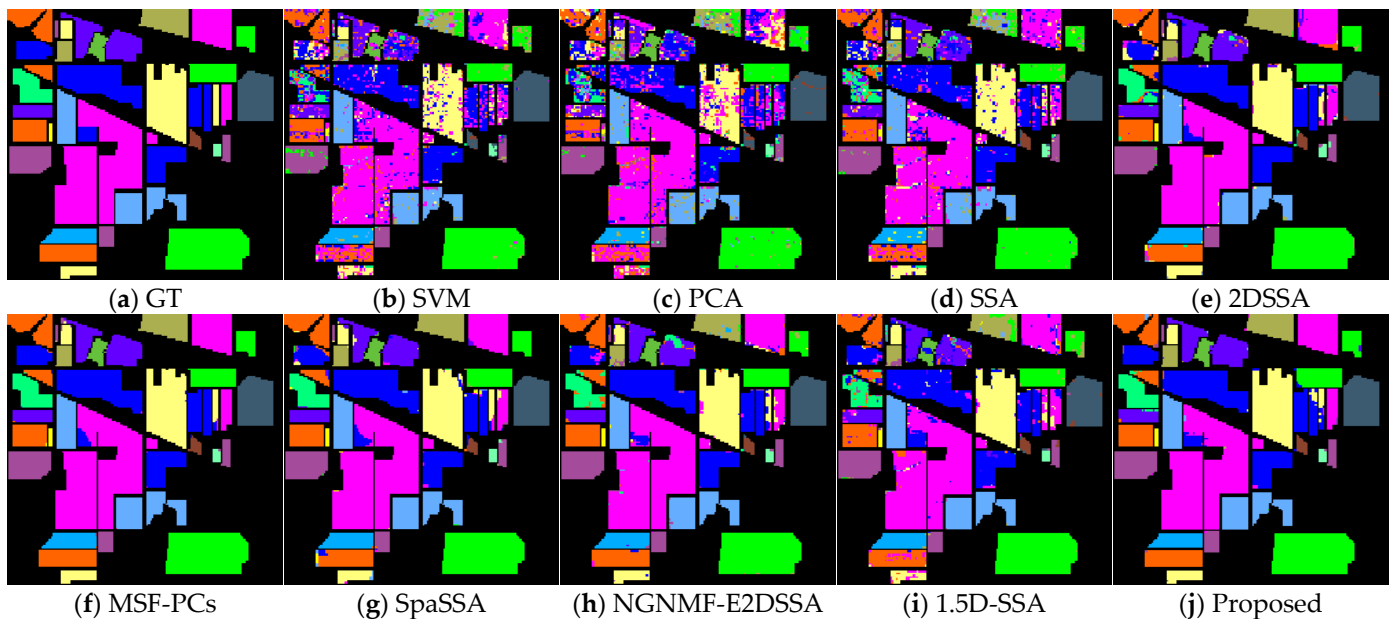pixel in the region on an arbitrarily shaped superpixel, demonstrating good edge-retention capability.

Figure 8. Classification results for the Indian Pines dataset.

To compare the classification performance of each algorithm more objectively, this paper uses four metrics: overall accuracy (OA), average accuracy (AA), and Kappa coefficient (Kappa) time consumed by classification (time) to measure the classification performance of the algorithms. OA refers to the number of correctly classified samples in the total test samples; AA represents the average of classification accuracy; Kappa provides information about the ground truth and mutual information about the strong agreement between the graph and the classification graph. The numerical results of the experiments on the three datasets are shown in Tables 2–4.

Table 2. Classification accuracy (%) for the Indian Pines dataset.

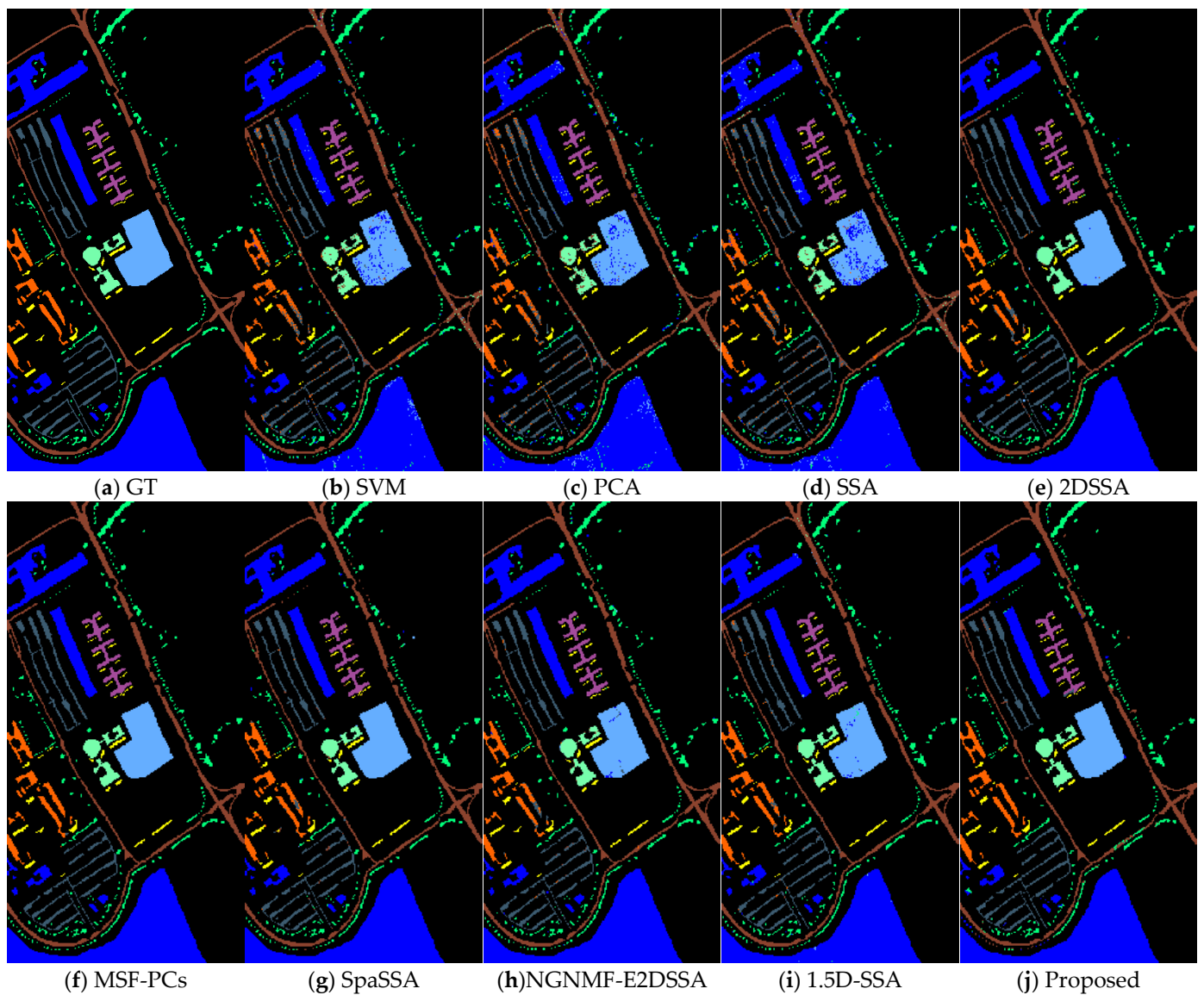| Class	Samples Train Set (%)	Test Set (%)	SVM	PCA	SSA	2DSSA	MSF-PCs	SpaSSA	NGNMF-E2DSSA	1.5D-SSA	Proposed
C1	8	92	11.9048	30.9524	76.1905	71.4286	95.2381	78.5714	88.0952	83.3333	97.619
C2	8	92	76.4661	67.4029	80.5788	92.3839	96.9535	93.6024	93.8309	92.3077	94.3524
C3	8	92	63.6959	54.5216	76.0157	93.4469	99.3447	95.675	96.3303	87.5491	97.0169
C4	8	92	31.6514	33.0275	53.6697	86.2385	99.5413	97.2477	88.0734	75.6881	99.0909
C5	8	92	83.1081	89.1892	93.6937	97.5225	99.7748	97.7477	98.6486	93.4685	95.7684
C6	8	92	91.5052	85.693	90.9091	97.7645	99.7019	99.5529	98.6587	99.2548	99.8525
C7	8	92	72	76	84	88	96	100	92	84	96.1538
C8	8	92	99.0888	94.7608	99.3166	98.4055	100	100	100	97.2665	100
C9	8	92	33.3333	16.6667	55.5556	100	100	100	100	94.4444	100
C10	8	92	71.4765	53.5794	82.2148	92.5056	97.5391	94.519	93.6242	88.4787	96.3455
C11	8	92	81.9752	75.775	83.8795	95.6156	99.7786	98.4942	96.5456	92.6484	99.4306
C12	8	92	57.4312	34.8624	72.6606	92.1101	97.9817	95.7798	87.5229	81.2844	97.6407
C13	8	92	92.0213	90.4255	91.4894	98.9362	98.4043	99.4681	97.8723	98.4043	99.4737
C14	8	92	93.8091	94.411	94.8409	98.9682	100	99.742	98.7102	97.3345	96.2585
C15	8	92	53.5211	46.7606	46.4789	94.9296	100	99.7183	89.8592	80	98.8827
C16	8	92	78.8235	91.7647	89.4118	100	100	100	100	82.3529	97.6744
OA (%)			77.8049	70.9797	83.0167	95.0218	99.0128	97.2827	95.5949	91.5296	97.5638
AA (%)			68.2382	64.737	79.4316	93.641	98.7661	96.8824	94.9857	89.2385	97.8475
Kappa*100			74.5235	66.6872	80.6055	94.327	98.8738	96.901	94.9776	90.3257	97.2222
Time (s)			2.235637	0.687991	4.153211	10.52716	10.69787	24.74259	13.23079	11.63065	1.133012

Figure 9. Classification results for the Pavia University dataset.

Table 3. Classification accuracy (%) for the Pavia University dataset.

Class	Samples Train Set (%)	Test Set (%)	SVM	PCA	SSA	2DSSA	MSF-PCs	SpaSSA	NGNMF-E2DSSA	1.5D-SSA	Proposed
C1	8	92	93.9672	94.3115	93.7377	99.1311	100	99.5246	99.541	99.0328	97.9344
C2	8	92	98.0591	96.9517	97.4588	100	100	99.9359	99.9942	99.761	99.7727
C3	8	92	80.5282	78.1978	78.3532	89.2284	99.0678	95.5463	90.2123	93.941	99.8446
C4	8	92	93.4705	89.5316	93.0092	97.0901	99.3612	92.1576	98.4031	99.3612	86.9056
C5	8	92	99.5958	99.8383	99.515	100	100	98.6257	99.3533	99.515	95.6346
C6	8	92	88.3485	89.6239	80.4367	99.7406	100	99.9135	98.0112	98.0329	99.8271
C7	8	92	87.408	83.8921	87.1627	95.4211	100	98.4464	95.3393	98.7735	100
C8	8	92	88.9283	84.0567	89.3416	96.5161	99.7638	97.0475	98.4057	97.2247	98.7009
C9	8	92	99.8852	100	99.8852	95.178	99.8852	92.1929	97.8186	99.8852	98.7371
OA (%)			94.0661	92.8717	92.7243	98.5489	99.8856	98.5896	98.7471	98.8767	98.338
AA (%)			92.2434	90.7115	90.9889	96.9228	99.7865	97.0434	97.4532	98.3919	97.4841
Kappa*100			92.1062	90.5243	90.2917	98.0746	99.8484	98.129	98.3371	98.5106	97.7937
Time (s)			5.296865	1.694653	21.8372	48.03557	156.9282	175.7011	115.4543	64.09886	2.84225

(**a**) GT   (**b**) SVM   (**c**) PCA   (**d**) SSA   (**e**) 2DSSA

(**f**) MSF-PCs   (**g**) SpaSSA   (**h**) NGNMF-E2DSSA   (**i**) 1.5D-SSA   (**j**) Proposed
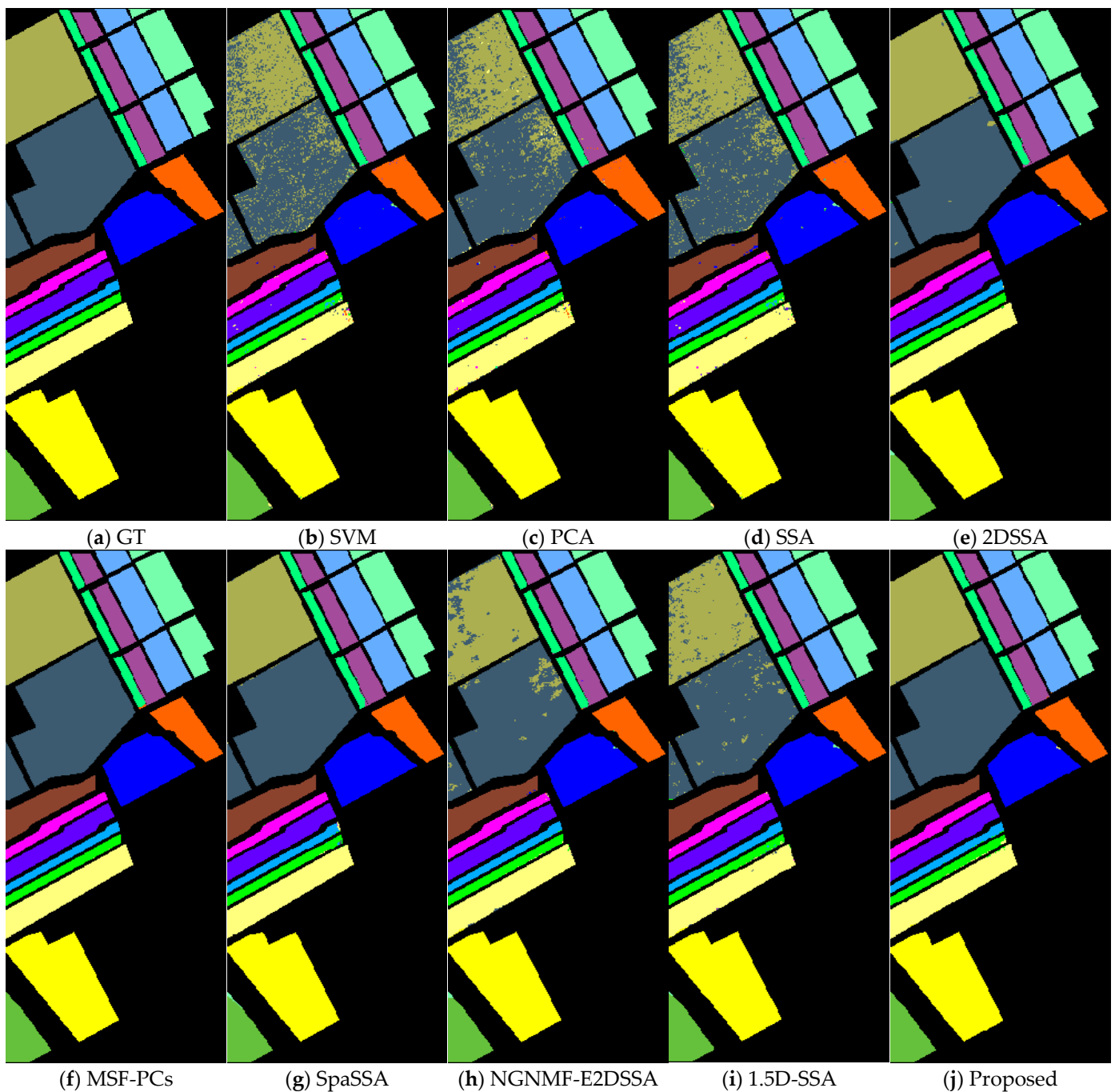
Figure 10. Classification results for the Salinas dataset.

As can be seen from Table 2, on the Indian Pines dataset, the proposed method has a significant improvement effect in extracting discriminative classification features compared with the traditional SSA algorithm and the 2DSSA algorithm, which extends to extract spatial information, and the overall classification accuracy, average classification accuracy, and Kappa coefficient are higher than the SVM algorithm by about 20% and higher than the traditional SSA algorithm by 14%. Above all, the proposed method achieved excessive smoothing of the input spectral vector by the traditional SSA. Only the trend of the spectral vector change can be retained, resulting in a lower classification effect. The proposed method is slightly higher than the other algorithms except for MSF-PCs in three measures of classification accuracy. In particular, it performs well in small-sample feature classification, such as the classification of Alfalfa, which has only 48 samples and

3–4 randomly selected samples in the training set, and the overall classification accuracy reaches 97.62%, which is much higher than that of the other methods in the table, indicating that the proposed method has excellent performance in small-sample classification tasks. In addition, the proposed method has a significant advantage in terms of running time. The NGNMF-E2DSSA algorithm, MSF-PCs algorithm, and 1.5D-SSA algorithm take more than 10 s to complete the classification on the Indian Pines dataset, and the SpaSSA algorithm takes 24 s, while the proposed method takes only 1.13 s to complete the classification with high accuracy. Since the WSA-SSA does not traverse every pixel operation with a fixed rectangular window, it directly deals with irregularly shaped superpixels, extracts spectral information and spatial structure information in the region, and reconstructs the superpixels, which significantly reduces the computational effort and shortens the running time.

Table 4. Classification accuracy (%) for the Salinas dataset.

Class	Samples Train Set (%)	Test Set (%)	SVM	PCA	SSA	2DSSA	MSF-PCs	SpaSSA	NGNMF-E2DSSA	1.5D-SSA	Proposed
C1	8	92	99.2965	99.2965	97.9978	100	100	100	99.5671	99.98918	100
C2	8	92	99.358	99.8249	99.358	99.8541	100	100	99.8249	99.9037	99.7666
C3	8	92	98.8442	99.0644	98.8442	99.8349	100	100	99.945	99.92845	100
C4	8	92	98.752	98.5179	98.2839	95.8658	97.5819	98.4399	99.22	99.39939	99.922
C5	8	92	99.6752	99.4316	99.7564	99.8782	100	99.8782	99.7158	99.25296	99.391
C6	8	92	99.7254	99.7529	99.6705	100	100	99.9725	99.8353	99.87369	99.9176
C7	8	92	99.9089	99.9696	99.9089	99.8177	100	99.9696	99.8785	99.76609	99.9089
C8	8	92	84.3572	87.7423	88.2149	99.4214	100	99.8264	95.2262	95.77392	100
C9	8	92	99.9299	99.9474	99.7897	100	100	100	100	99.7669	100
C10	8	92	96.9154	95.9536	97.0481	99.403	100	99.9005	98.5406	98.5373	99.1708
C11	8	92	98.0652	97.9633	98.4725	99.1853	100	99.8982	99.1853	99.18534	100
C12	8	92	99.5485	99.8871	99.5485	99.8307	100	100	100	99.98307	100
C13	8	92	99.6437	99.6437	99.2874	99.6437	100	97.1496	98.9311	99.12113	97.7435
C14	8	92	93.1911	97.1545	93.3943	99.8984	99.6951	97.8659	98.2724	98.32316	95.7317
C15	8	92	75.9198	70.4906	78.4026	99.2671	99.9701	99.8654	90.0688	93.4116	99.9103
C16	8	92	99.278	98.9771	99.278	99.1576	100	98.2551	98.8568	99.20578	100
OA (%)			92.9081	92.9342	93.9826	99.5461	99.9277	99.7389	97.393	97.94192	99.755
AA (%)			96.4006	96.4761	96.7035	99.4411	99.8279	99.4388	98.5667	98.83887	99.4664
Kappa*100			92.102	92.123	93.2961	99.4945	99.9195	99.7092	97.0958	97.7082	99.7271
Time (s)			15.05047	3.013788	24.47528	54.02874	80.92167	203.3935	69.76287	58.79197	2.714727

It can be visualized from Tables 3 and 4 that the overall classification accuracy of the window shape adaptive SSA algorithm can reach 98.34% and 99.77% on the Pavia University dataset and Salinas dataset; the average classification accuracy reaches 97.79% and 99.46%, respectively; and the corresponding Kappa coefficients are high, showing good performance. An accuracy of 100% can be achieved in the classification of some categories of features. Similarly, it can be seen in Tables 3 and 4 that the proposed method can achieve more than 99.5% accuracy in the classification of small sample feature categories. In addition, due to the larger spatial dimensions of both the Pavia University dataset and the Salinas dataset over the Indian Pines dataset, the computational effort of each algorithm in the table increases and the running time becomes significantly longer. The running time of the NGNMF-E2DSSA algorithm, SpaSSA algorithm, and MSF-PCs algorithm on the Pavia University data set takes more than 100 s, while the proposed method in this paper takes only 2.84 s. On the Salinas dataset, the WSA-SSA also takes only 2.71 s to finish the classification, which is far ahead of the other algorithms. The advantage of WSA-SSA in reducing the computational effort is more prominent in large-size images, where it can achieve fast classification results. The proposed method has potential applications in other fields, such as holographic displays [46,47], image compression [48,49], optical imaging [50–52], etc.

5. Conclusions

This paper analyzes the characteristics of hyperspectral images as a three-dimensional data cube containing millions of pixels; the volume of data processing is substantial, leading to an extended processing duration. Introducing the WSA-SSA algorithm, it is crafted to simultaneously extract spectral features and local spatial features. The algorithm dynamically adjusts to diverse window shapes, a pivotal capability for alleviating misclassification at the boundaries of different species, particularly when dealing with irregular shapes within feature regions. This results in better and more accurate classification of boundary pixels. Importantly, the algorithm does not employ a fixed window for iterating over each pixel, reducing computational complexity. Moreover, a classification algorithm based on WSA-SSA is introduced. It partitions hyperspectral images based on spatial information; employs the WSA-SSA algorithm for spectral and spatial feature extraction; and, finally, combines SVM for feature classification. This approach achieves high-precision classification on three benchmark datasets while significantly reducing the classification time. Although WSA-SSA demonstrates excellent performance on these datasets, it focuses solely on spectral and local spatial information during feature extraction, neglecting global spatial information. In future work, the 2DSSA algorithm could be introduced to consider global spatial information and enhance classification accuracy.

Author Contributions: Conceptualization, X.B. and G.L.; methodology, X.B.; software, X.B. and B.Q.; validation, X.B., B.Q. and J.L.; formal analysis, J.L.; data curation, X.B. and L.J.; writing—original draft preparation, X.B.; writing—review and editing, G.L., B.Q. and J.L; project management, G.L. and J.L. All authors have read and agreed to the published version of the manuscript.

Data Availability Statement: Data are contained within the article.

Conflicts of Interest: The authors declare no conflict of interest.

References

1. AVHYAS: A Free and Open Source QGIS Plugin for Advanced Hyperspectral Image Analysis. In Proceedings of the 2021 International Conference on Emerging Techniques in Computational Intelligence (ICETCI), Hyderabad, India, 25–27 August 2021; pp. 71–76.
2. Song, X.; Sunil, A.; Kai, M.T.; Zhen, L.; Bin, H. Spectral-Spatial Anomaly Detection of Hyperspectral Data Based on Improved Isolation Forest. *IEEE Trans. Geosci. Remote Sens.* **2022**, *60*, 1–16. [CrossRef]
3. Li, H. An Overview on Remote Sensing Image Classification Methods with a Focus on Support Vector Machine. In Proceedings of the 2021 International Conference on Signal Processing and Machine Learning (CONF-SPML), Stanford, CA, USA, 14 November 2021; pp. 50–56.
4. Liu, H.; Li, W.; Xia, X.-G.; Zhang, M.; Gao, C.-Z.; Tao, R. Central Attention Network for Hyperspectral Imagery Classification. *IEEE Trans. Neural Netw. Learn. Syst.* **2022**, *34*, 8989–9003. [CrossRef] [PubMed]
5. Rasti, B.; Hong, D.; Hang, R.; Ghamisi, P.; Kang, X.; Chanussot, J.; Benediktsson, J.A. Feature extraction for hyperspectral imagery: The evolution from shallow to deep: Overview and toolbox. *IEEE Geosci. Remote Sens. Mag.* **2020**, *8*, 60–88. [CrossRef]
6. Peng, J.; Sun, W.; Du, Q. Self-paced joint sparse representation for the classification of hyperspectral images. *IEEE Trans. Geosci. Remote Sens.* **2018**, *57*, 1183–1194. [CrossRef]
7. Su, H.; Yong, B.; Du, P.; Liu, H.; Chen, C.; Liu, K. Dynamic classifier selection using spectral-spatial information for hyperspectral image classification. *J. Appl. Remote Sens.* **2014**, *8*, 085095. [CrossRef]
8. Tyo, J.S.; Konsolakis, A.; Diersen, D.I.; Olsen, R.C. Principal-components-based display strategy for spectral imagery. *IEEE Trans. Geosci. Remote Sens.* **2003**, *41*, 708–718. [CrossRef]
9. Chiu, S.-H.; Lu, C.-P.; Wu, D.-C.; Wen, C.-Y. A histogram based data-reducing algorithm for the fixed-point independent component analysis. *Pattern Recognit. Lett.* **2008**, *29*, 370–376. [CrossRef]
10. Chen, M.; Wang, Q.; Li, X. Discriminant Analysis with Graph Learning for Hyperspectral Image Classification. *Remote. Sens.* **2018**, *10*, 836. [CrossRef]
11. Guan, L.; Xie, W.; Pei, J. Segmented minimum noise fraction transformation for efficient feature extraction of hyperspectral images. *BPRA Int. Conf. Pattern Recognit.* **2015**, *48*, 3216–3226.
12. Bachmann, C.M.; Ainsworth, T.L.; Fusina, R.A. Exploiting manifold geometry in hyperspectral imagery. *IEEE Trans. Geosci. Remote Sens.* **2005**, *43*, 441–454. [CrossRef]
13. Li, B.; Li, Y.-R.; Zhang, X.-L. A survey on Laplacian eigenmaps based manifold learning methods. *Neurocomputing* **2019**, *335*, 336–351. [CrossRef]

14. Roweis, S.T.; Saul, L.K. Nonlinear Dimensionality Reduction by Locally Linear Embedding. *Science* **2000**, *290*, 2323–2326. [CrossRef] [PubMed]

15. Zabalza, J.; Ren, J.; Wang, Z.; Marshall, S.; Wang, J. Singular Spectrum Analysis for Effective Feature Extraction in Hyperspectral Imaging. *IEEE Geosci. Remote Sens. Lett.* **2014**, *11*, 1886–1890. [CrossRef]

16. Benediktsson, J.A.; Pesaresi, M.; Arnason, K. Classification and feature extraction for remote sensing images from urban areas based on morphological transformations. *IEEE Trans. Geosci. Remote Sens.* **2003**, *41*, 1940–1949. [CrossRef]

17. Benediktsson, J.A.; Palmason, J.A.; Sveinsson, J.R. Classification of hyperspectral data from urban areas based on extended morphological profiles. *IEEE Trans. Geosci. Remote Sens.* **2005**, *43*, 480–491. [CrossRef]

18. Mauro, D.M.; Jon, A.B.; Björn, W.; Lorenzo, B. Morphological Attribute Profiles for the Analysis of Very High Resolution Images. *IEEE Trans. Geosci. Remote Sens.* **2010**, *48*, 3747–3762.

19. Mauro, D.M.; Alberto, V.; Jon, A.B.; Jocelyn, C.; Lorenzo, B. Classification of Hyperspectral Images by Using Extended Morphological Attribute Profiles and Independent Component Analysis. *IEEE Geosci. Remote Sens. Lett.* **2011**, *8*, 542–546.

20. Welch, R.M.; Sengupta, S.K.; Chen, D.W. Cloud field classification based upon high spatial resolution textural features: 1. Gray level co-occurrence matrix approach. *J. Geophys. Res.* **1988**, *93*, 12663–12681. [CrossRef]

21. Kim, S.-D.; Udpa, S. Texture classification using rotated wavelet filters. *IEEE Trans. Syst. Man Cybern. Syst.* **2000**, *30*, 847–852.

22. Jia, S.; Lin, Z.; Deng, B.; Zhu, J.; Li, Q. Cascade Superpixel Regularized Gabor Feature Fusion for Hyperspectral Image Classification. *IEEE Trans. Neural Netw.* **2020**, *31*, 1638–1652. [CrossRef]

23. Yan, S.; Xu, D.; Zhang, B.; Zhang, H.J.; Yang, Q.; Lin, S. Graph Embedding and Extensions: A General Framework for Dimensionality Reduction. *IEEE Trans. Pattern Anal. Mach. Intell.* **2007**, *29*, 40–51. [CrossRef] [PubMed]

24. Zabalza, J.; Ren, J.; Zheng, J.; Han, J.; Zhao, H.; Li, S.; Marshall, S. Novel Two-Dimensional Singular Spectrum Analysis for Effective Feature Extraction and Data Classification in Hyperspectral Imaging. *IEEE Trans. Geosci. Remote Sens.* **2015**, *53*, 4418–4433. [CrossRef]

25. Hang, F.; Sun, G.; Zabalza, J.; Zhang, A.; Ren, J.; Jia, X. A Novel Spectral-Spatial Singular Spectrum Analysis Technique for Near Real-Time In Situ Feature Extraction in Hyperspectral Imaging. *IEEE J. Sel. Top. Appl. Earth Obs. Remote Sens.* **2020**, *13*, 2214–2225.

26. Hang, F.; Sun, G.; Ren, J.; Zhang, A.; Jia, X. Fusion of PCA and Segmented-PCA Domain Multiscale 2-D-SSA for Effective Spectral-Spatial Feature Extraction and Data Classification in Hyperspectral Imagery. *IEEE Trans. Geosci. Remote Sens.* **2022**, *60*, 1–14.

27. Sun, G.; Hang, F.; Ren, J.; Zhang, A.; Zabalza, J.; Jia, X.; Zhao, H. SpaSSA: Superpixelwise Adaptive SSA for Unsupervised Spatial–Spectral Feature Extraction in Hyperspectral Image. *IEEE Trans. Cybern.* **2022**, *52*, 6158–6169. [CrossRef] [PubMed]

28. Swalpa, K.R.; Gopal, K.; Shiv, R.D.; Bidyut, B.C. HybridSN: Exploring 3-D-2-D CNN Feature Hierarchy for Hyperspectral Image Classification. *Comput. Res. Repos.* **2020**, *17*, 277–281.

29. Hang, R.; Li, Z.; Liu, Q.; Ghamisi, P.; Bhattacharyya, S.S. Hyperspectral Image Classification with Attention-Aided CNNs. *IEEE Trans. Geosci. Remote Sens.* **2021**, *59*, 2281–2293. [CrossRef]

30. Mei, X.; Pan, E.; Ma, Y.; Dai, X.; Huang, J.; Fan, F.; Du, Q.; Zheng, H.; Ma, J. Spectral-Spatial Attention Networks for Hyperspectral Image Classification. *Remote Sens.* **2019**, *11*, 963. [CrossRef]

31. Lee, H.; Kwon, H. Going Deeper with Contextual CNN for Hyperspectral Image Classification. *IEEE Trans. Image Process.* **2017**, *26*, 4843–4855. [CrossRef]

32. Hong, D.; Han, Z.; Yao, J.; Gao, L.; Zhang, B.; Plaza, A.; Chanussot, J. SpectralFormer: Rethinking Hyperspectral Image Classification with Transformers. *IEEE Trans. Geosci. Remote Sens.* **2022**, *60*, 1–15. [CrossRef]

33. Vautard, R.; Yiou, P.; Ghil, M. Singular-spectrum analysis: A toolkit for short, noisy chaotic signals. *Phys. D Nonlinear Phenom.* **1992**, *58*, 95–126. [CrossRef]

34. Zhong, Z.; Li, Y.; Ma, L.; Li, J.; Zheng, W.S. Spectral–spatial transformer network for hyperspectral image classification: A factorized architecture search framework. *IEEE Trans. Geosci. Remote Sens.* **2021**, *60*, 1–15. [CrossRef]

35. Danilov, D.; Zhiglyavskii, A. *Principal Components of Time Series: The 'Caterpillar' Method*; St. Petersburg University: Saint Petersburg, Russia, 1997. Available online: http://www.gistatgroup.com/cat/books.html (accessed on 1 October 2022). (In Russian)

36. Golyandina, N.E.; Usevich, K.D. 2D-extension of Singular Spectrum Analysis: Algorithm and elements of theory. In *Matrix Methods: Theory, Algorithms and Applications: Dedicated to the Memory of Gene Golub*; World Scientific: Singapore, 2010; pp. 449–473.

37. Rodríguez-Aragón, L.J.; Zhigljavsky, A. Singular spectrum analysis for image processing. *Stat. Its Interface* **2010**, *3*, 419–426. [CrossRef]

38. Ren, X.; Malik, J. Learning a classification model for segmentation. In Proceedings of the IEEE International Conference on Computer Vision, Nice, France, 13–16 October 2003; Volume 1, pp. 10–17.

39. Liu, M.-Y.; Tuzel, O.; Ramalingam, S.; Chellappa, R. Entropy rate superpixel segmentation. *Comput. Vis. Pattern Recognit.* **2011**, *2011*, 2097–2104.

40. Luo, F.; Zhang, L.; Zhou, X.; Guo, T.; Cheng, Y.; Yin, T. Sparse-Adaptive Hypergraph Discriminant Analysis for Hyperspectral Image Classification. *IEEE Geosci. Remote Sens. Lett.* **2020**, *17*, 1082–1086. [CrossRef]

41. Archibald, R.; Fann, G. Feature Selection and Classification of Hyperspectral Images with Support Vector Machines. *IEEE Geosci. Remote Sens. Lett.* **2007**, *4*, 674–677. [CrossRef]

42. Hyperspectral Data Set [OL]. Available online: http://www.ehu.eus/ccwintco/index.php?title=Hyperspectral_Remote_Sensing_Scenes (accessed on 1 October 2022).

43. Fu, H.; Zhang, A.; Sun, G.; Ren, J.; Jia, X.; Pan, Z.; Ma, H. A Novel Band Selection and Spatial Noise Reduction Method for Hyperspectral Image Classification. *IEEE Trans. Geosci. Remote Sens.* **2022**, *60*, 5535713. [CrossRef]

44. Zhao, X.; Liu, K.; Gao, K.; Li, W. Hyperspectral Time-Series Target Detection Based on Spectral Perception and Spatial–Temporal Tensor Decomposition. *IEEE Trans. Geosci. Remote Sens.* **2023**, *61*, 5520812. [CrossRef]

45. Zhao, X.; Li, W.; Zhao, C.; Tao, R. Hyperspectral Target Detection Based on Weighted Cauchy Distance Graph and Local Adaptive Collaborative Representation. *IEEE Trans. Geosci. Remote Sens.* **2022**, *60*, 5527313. [CrossRef]

46. Li, J.; Smithwick, Q.; Chu, D. Holobricks: Modular coarse integral holographic displays. *Light Sci. Appl.* **2022**, *11*, 57. [CrossRef]

47. Li, J.; Smithwick, Q.; Chu, D. Bandwidth utilization improvement methods of Coarse Integral Holographic video displays. In *Imaging and Applied Optics 2018 (3D, AO, AIO, COSI, DH, IS, LACSEA, LS&C, MATH, pcAOP), OSA Technical Digest*; Optica Publishing Group: Washington, DC, USA, 2018; Paper DTh3D.6.

48. Li, J.; Liu, Z. Multispectral transforms using convolution neural networks for remote sensing multispectral image compression. *Remote Sens.* **2019**, *11*, 759. [CrossRef]

49. Li, J.; Liu, Z. Efficient compression algorithm using learning networks for remote sensing images. *Appl. Soft Comput.* **2021**, *100*, 106987. [CrossRef]

50. Tehseen, R.; Ali, A.; Mane, M.; Ge, W.; Li, Y.; Zhang, Z.; Xu, J. Enhanced imaging through turbid water based on quadrature lock-in discrimination and retinex aided by adaptive gamma function for illumination correction. *Chin. Opt. Lett.* **2023**, *21*, 101102. [CrossRef]

51. Park, Y.S.; Hong, J.; Choi, J. X-ray volumetric quantitative phase imaging by Foucault differential filtering with linear scanning. *Chin. Opt. Lett.* **2023**, *21*, 013401. [CrossRef]

52. Li, J.; Liu, Z. High-resolution dynamic inversion imaging with motion-aberrations-free using optical flow learning networks. *Sci. Rep.* **2019**, *9*, 11319. [CrossRef]